npj | Quantum Information

www.nature.com/npjqi

ARTICLE OPEN

Loading a quantum-dot based “Qubyte” register

C. Volk[1], A. M. J. Zwerver[1], U. Mukhopadhyay[1], P. T. Eendebak[2], C. J. van Diepen[1], J. P. Dehollain[1], T. Hensgens[1], T. Fujita[1,4], C. Reichl[3], W. Wegscheider[3] and L. M. K. Vandersypen[1]

Electrostatically defined quantum dot arrays offer a compelling platform for quantum computation and simulation. However, tuning up such arrays with existing techniques becomes impractical when going beyond a handful of quantum dots. Here, we present a method for systematically adding quantum dots to an array one dot at a time, in such a way that the number of electrons on previously formed dots is unaffected. The method allows individual control of the number of electrons on each of the dots, as well as of the interdot tunnel rates. We use this technique to tune up a linear array of eight GaAs quantum dots such that they are occupied by one electron each. This new method overcomes a critical bottleneck in scaling up quantum-dot based qubit registers.

npj Quantum Information (2019)5:29 ; https://doi.org/10.1038/s41534-019-0146-y

INTRODUCTION

Quantum-dot based electron spin qubit systems[1–3] have made significant steps towards becoming a scalable platform for quantum computation. Important landmarks include the realization of 99.9%-fidelity single-qubit gates,[4] the implementation of two-qubit gates[5–10] and two-qubit algorithms.[11] Although a high degree of control of the charge and spin degrees of freedom has been shown, research has been mainly limited to single, double and triple dot systems. Recently, control of the charge occupation of four dot systems has been demonstrated[12–15] and a single electron could be controllably placed in a 3×3 array.[16] However, device specific approaches to tuning quantum dots will need to be replaced by a systematic approach, as arrays become larger with the scale-up of quantum-dot based quantum circuits.

The controlled formation and filling of large quantum dot (QD) arrays poses multiple challenges. Individual gate voltages affect not only the parameter they are designed to control, typically the electrochemical potential of a specific QD or the tunnel barrier between two adjacent QDs, but through capacitive cross-talk also affect other electrochemical potentials and tunnel barriers.[17] Furthermore, tuning devices is complicated by a disordered potential landscape arising from charges trapped in randomly located impurities and defects in the substrate and at the surface.[18,19] Finally, electrons are loaded into QDs from an electron reservoir. When a target dot is separated from the reservoir by one or more other dots, electrons are typically loaded by co-tunneling, only virtually occupying the intermediate dots. However, for more than three or four dots, the co-tunnel rates become impractically low.

These challenges present themselves when measuring the charge occupation in quantum dot arrays through conventional charge stability diagrams. In such diagrams, the signal from a charge sensor is recorded while sweeping two gate voltages, resulting in a 2D plot that exhibits regions in gate voltage space with a fixed number of electrons on each dot, separated by lines indicating charge additions to the array, or charge transitions between dots.[17] Such a 2D plot corresponds to a plane in a multi-dimensional space spanned by all the gate voltages. As arrays get larger, when sweeping just two gate voltages, cross-talk leads to slopes of charge transition lines that are almost parallel and hard to distinguish. Assignment of charge transition lines to specific dots is further complicated by non-uniform addition energies. Furthermore, the intersections between different charge addition lines can cluster together in a small gate voltage region. Finally, the difficulty of loading electrons to dots far from the reservoir leads to postponed loading of dots (latching) or to missing charge addition lines.[20] Those complications lead to plots that are difficult to interpret.[21]

Cross-talk and the background disorder potential have been compensated for in short dot arrays using so called virtual gates, which are linear combinations of multiple gate voltages chosen such that only a single electrochemical potential or tunnel barrier is addressed.[22] Virtual gates also make it possible to strategically choose the measured 2D plane in gate-space, such that multi-dot charge stability diagrams become easy to interpret.[16,22,23] The difficulty of loading electrons into large arrays has been circumvented using additional reservoirs in between groups of three dots.[24] In another approach, an additional access point to a reservoir was created halfway a linear array of five QDs.[21] Instead of loading electrons by co-tunneling, electrons can also be made to sequentially tunnel through a chain of dots to reach their target location,[25] but this approach requires the chain of dots to be already formed in the first place.

We explored several approaches to form long linear arrays in a controlled way, such as forming individual single dots first and stitching them together, stitching together double dots, or starting with a large QD and then splitting it up into an array of separate dots. However, we found it difficult to make these approaches work well.

Here, we show the controlled filling of an array of eight QDs, which we call a Qubyte register, using a method that is both

---

[1]QuTech and Kavli Institute of Nanoscience, TU Delft, 2600 GA Delft, The Netherlands; [2]QuTech and Netherlands Organization for Applied Scientific Research (TNO), 2600 AD Delft, The Netherlands; [3]Solid State Physics Laboratory, ETH Zürich, 8093 Zürich, Switzerland; [4]Present address: The Institute of Scientific and Industrial Research, Osaka University, Ibaraki, Osaka, Japan
Correspondence: L M. K. Vandersypen (l.m.k.vandersypen@tudelft.nl)
These authors contributed equally: C. Volk, A. M. J. Zwerver

Received: 27 December 2018 Accepted: 2 April 2019
Published online: 23 April 2019

conceptually simple and effective. Starting from a double dot, we introduce the "$n+1$ method", adding dots one by one using virtual gates. Every new dot added adjacent to the existing array is right next to a reservoir so the dot can be filled easily. The use of virtual gates saves the charge occupation in the previously formed dots while adding a new dot, and also keeps the charge stability diagrams simple to interpret. (In the course of preparing this manuscript, we became aware of closely related work on a linear array of nine Si/SiGe QDs, see ref. [26]) We show that we can locally control the number of electrons on each dot down to the last electron, and that we can set all interdot tunnel couplings to typical values used in spin qubit experiments. Finally, we discuss the limitations and potential pitfalls of the $n+1$ method.

RESULTS

Device and initial characterization

Figure 1a shows a scanning electron micrograph of a device nominally identical to the one used in the experiment. The gate layout has been adapted from previous triple and quadruple quantum dot devices.[14,23] On one side, 17 gates with a pitch of 80 nm are fabricated to control the tunnel barriers and electrochemical potentials of the QDs. The upper part of the sample accommodates two sensing dots (SD) that are capacitively coupled to the linear QD array. The circles indicate the intended positions of the QDs. All measurements are carried out in a dilution refrigerator with a base temperature below 20 mK.

Initially, the device is characterized by DC transport measurements. The pinch-off characteristics of the channel between each of the plunger P_i or barrier B_i gates and the central gate D is measured (see schematics in Fig. 1a) and single QDs are formed by sweeping pairs of neighboring barrier gates. These measurements confirm that all QDs, including the sensing dots, can be formed (if not, the sample is considered unsuitable to host eight QDs). Moreover, the pinch-off values determined for each gate act as starting parameters for further tuning. In all subsequent measurements, we probe the linear QD array via the two sensing dots, which are sensitive to the number of electrons in the array, as well as to their position in the array. The charge sensors are probed using RF reflectometry (see Methods section).

To illustrate the difficulty of traditional tuning strategies, Fig. 1b shows a charge stability diagram for a linear six-dot array (sextuple dot) confined between the barrier gates B_1 to B_7. The charge stability diagram has been recorded sweeping the voltages of gates P_2 and P_7, i.e., the gates mostly coupled to the outer QDs. In the diagram, charge addition lines with different slopes can be identified. However, charge transitions with similar slopes can only be assigned unambiguously to specific dots, after also stepping other gate voltages (see e.g., the small difference in slope between the transitions for dots 6 and 7). Even then, the complex pattern of transitions in the center of the diagram makes it extremely difficult to determine the charge occupation at every point in this gate space. Moreover, cross-capacitances hinder local tuning of the electrochemical potential and tunnel rates.

$n+1$ method

To tune up a multi-dot array dot by dot, we make use of virtual gates, which compensate for the cross-talk on the electrochemical

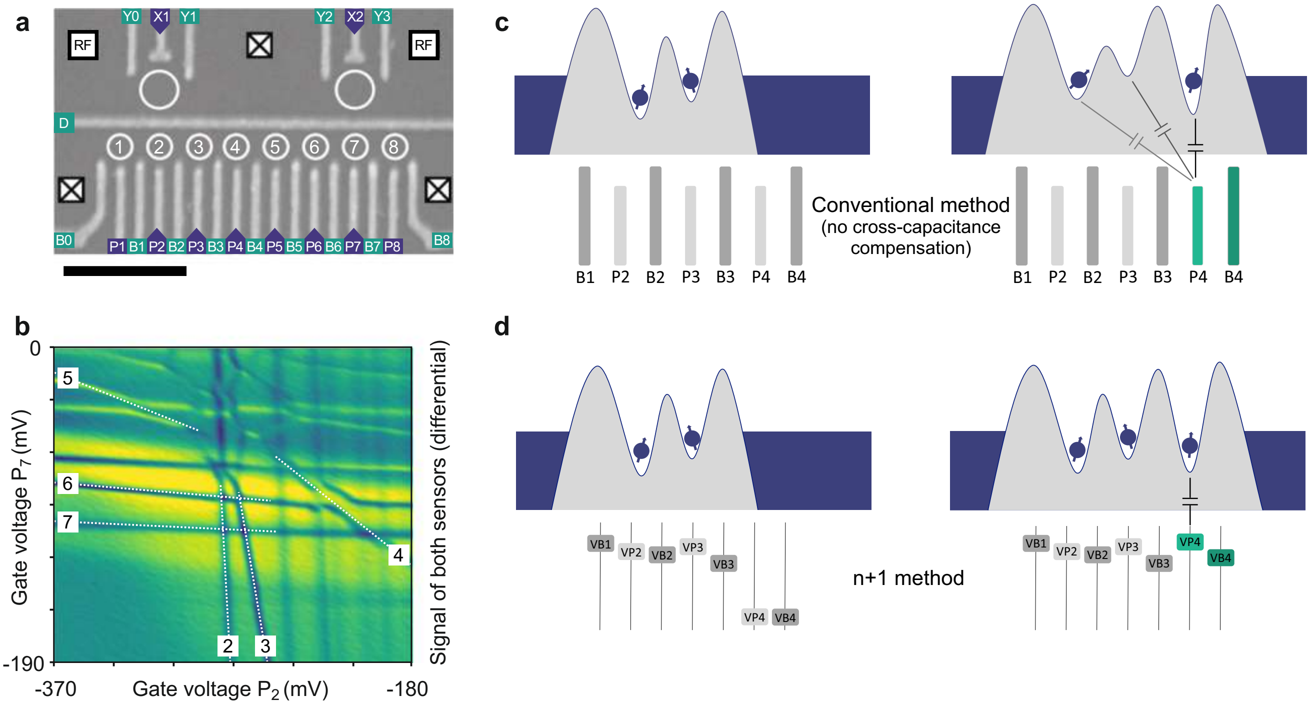
a
Y0
X1
Y1
Y2
X2
Y3
RF
RF
D
1
2
3
4
5
6
7
8
B0
P1 B1 P2 B2 P3 B3 P4 B4 P5 B5 P6 B6 P7 B7 P8
B8
b
0
5
6
7
4
2
3
-190
-370
Gate voltage P$_2$ (mV)
-180
Gate voltage P$_7$ (mV)
Signal of both sensors (differential)
c
B1 P2 B2 P3 B3 P4 B4
Conventional method
(no cross-capacitance compensation)
B1 P2 B2 P3 B3 P4 B4
d
VB1 VP2 VB2 VP3 VB3 VP4 VB4
n+1 method
VB1 VP2 VB2 VP3 VB3 VP4 VB4

Fig. 1 Device design and tuning principle. **a** Scanning electron micrograph of a device nominally identical to the one used in the experiment. The scale bar measures 500 nm. The circles indicate the intended positions of eight quantum dots (QDs) that define a Qubyte register and of two additional dots that are used for charge sensing. For the linear array, the designed dot-to-dot pitch is 160 nm. The plunger gates connected to high-frequency lines are marked with blue triangles. The white squares indicate the position of the Fermi reservoirs. Two on-board tank circuits for RF reflectometry readout are connected to each of the sensing dots. **b** Charge stability diagram of a sextuple dot formed between barrier gates B_1 and B_7. The sum of the differential demodulated voltages of both sensing dots is plotted. The dashed lines highlight charge transitions of each of the six QDs (the numbers refer to the labels in **a**). **c** Illustration of the potential landscape of a double QD. Gates P_4 and B_4 are used to form a third QD. Capacitive cross-talk, indicated by the capacitor symbols, has not been compensated for. Thus, these gates influence the potential of the other QDs as well (to avoid clutter, we did not draw any other capacitor symbols). **d** A double QD is extended to a triple QD using the virtual plunger VP_4 and barrier VB_4. Due to cross-capacitance compensation, these parameters only act locally on the potential landscape

potentials that occurs when sweeping actual gate voltages (see Fig. 1c, d). The virtual gates as used here do not compensate for cross-talk effects on tunnel barriers. The virtual plunger gate VP_i directly corresponds to the electrochemical potential of QD_i, up to a lever arm. The compensation is performed to first order, so that we can express the virtual gates as linear combinations of the physical gate voltages, summarized by a cross-capacitance matrix.[5,22]

The tuning procedure consists of the following steps, described in more detail below:

1. Tune up a double quantum dot (DQD) and one sensing dot with the traditional strategy.
2. Measure the cross-capacitance between all gates and the electrochemical potentials of these three QDs and record them in a cross-capacitance matrix. This matrix can now be used to generate virtual gates.
3. Use the virtual plunger and barrier gates adjacent to the existing dots to form the next QD without disturbing the former.
4. Measure the cross-capacitance between all gates and the electrochemical potential of the newly formed QD and place these values in the corresponding row of the matrix.
5. Re-measure the cross-capacitances to the previously formed QDs and update the matrix accordingly.

Steps 3–5 are repeated to extend the array, adding one QD at a time.

Before we describe these five steps in more detail, we first explain how the cross-capacitance matrix $A = (\alpha_{ij})$ is used to create virtual gates. For illustration purposes, we do this for the first three dots, leaving out the outer barrier gates and the gates of the sensing dots for simplicity. The following relationship expresses how much each physical gate affects each virtual gate:

$$\begin{pmatrix} \Delta VP_1 \\ \Delta VB_1 \\ \Delta VP_2 \\ \Delta VB_2 \\ \Delta VP_3 \end{pmatrix} = \begin{pmatrix} 1 & \alpha_{12} & \alpha_{13} & \alpha_{14} & \alpha_{15} \\ 0 & 1 & 0 & 0 & 0 \\ \alpha_{31} & \alpha_{32} & 1 & \alpha_{34} & \alpha_{35} \\ 0 & 0 & 0 & 1 & 0 \\ \alpha_{51} & \alpha_{52} & \alpha_{53} & \alpha_{54} & 1 \end{pmatrix} \begin{pmatrix} \Delta P_1 \\ \Delta B_1 \\ \Delta P_2 \\ \Delta B_2 \\ \Delta P_3 \end{pmatrix} \quad (1)$$

For convenience, we set the diagonal entries to 1 (dimensionless), disregarding the lever arm. This implies we express virtual gates in units of Volt, similar to the physical gates. Furthermore, since we do not include cross-talk effects on tunnel barriers, the off-diagonal matrix elements relating the physical gate voltages to virtual barrier gates are set to zero. The inverse matrix expresses the linear combination of physical gate voltages that is needed to sweep a virtual gate. We note that the diagonal entries of the inverse matrix do not need to be equal to 1.

We now turn to the five steps in the $n + 1$ method. In step 1, we form QD_2, QD_3 and the left sensing dot using conventional methods. The resulting charge stability diagram is shown in Fig. 2a. The matrix A_1 at this point is simply the identity matrix (this matrix and the matrices produced in subsequent steps are shown in the Supplementary information). For step 2, the matrix entries for QD_2, QD_3 and the left sensing dot are determined by recording how much an addition line for QD_i in a P_i scan is displaced when stepping any of the other plunger (barrier) gates P_j (B_j) by an amount δV (see Supplementary Fig. S1). The ratio of the shift of the charge transition line of QD_i in the P_i scan and δV yields the corresponding entry in the cross-capacitance matrix. We do this for all eight plunger and nine barrier gates of the linear array, as well as for the plunger gates of both sensing dots. The resulting matrix is A_2.

The effectiveness of the cross-talk compensation can be seen by recording a charge stability diagram in the virtual gate space, i.e., using VP_2 and VP_3 as sweep parameters (see Fig. 2b). Ideally, addition lines of QD_2 and QD_3 appear as orthogonal (horizontal and vertical) lines. In practice, the compensation is not always perfect because we extrapolate each cross-capacitance from just two data points (see Supplementary Fig. S1), but it is usually good enough.

To add the next QD (step 3), here QD_4, we form a new tunnel barrier using the neighboring virtual barrier gate, VB_4. The pinch-off values determined in DC transport indicate a suitable voltage range to scan with the barrier gate. Optionally, we then monitor the charge stability diagram VP_2—VP_3 while stepping VB_4. Once the barrier is raised sufficiently to form an additional QD, new addition lines appear in the charge stability diagram (see arrows in Fig. 2c). The charge transitions of the previously tuned QDs are

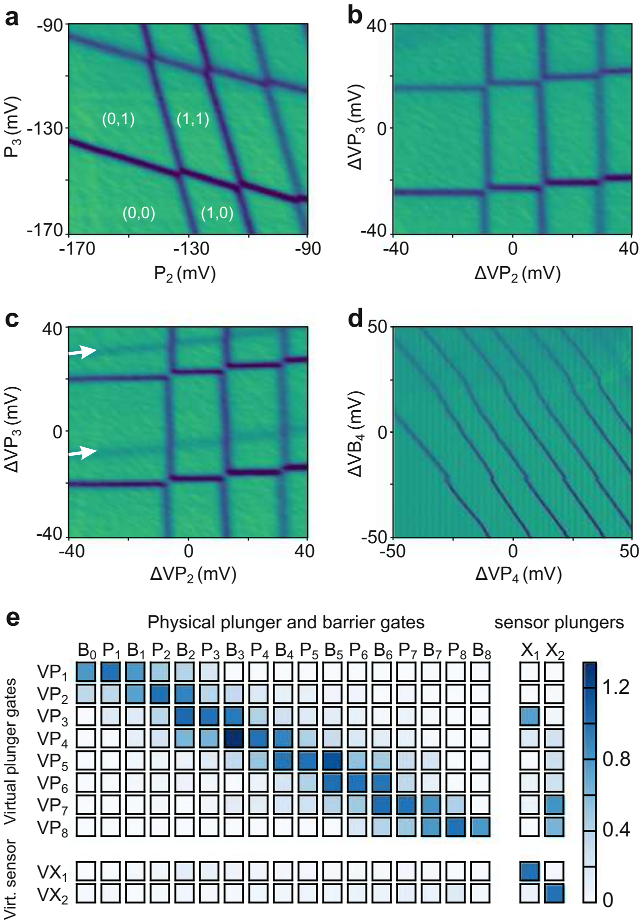

Fig. 2 Tuning method. **a** Charge stability diagram of a DQD in the single electron regime. The charge sensor response (the differential demodulated voltage, in arbitrary units, is plotted here and in similar plots below) is plotted as a function of the plunger gate voltages P_2 and P_3. **b** Charge stability diagram of the same DQD recorded as a function of the virtual plungers VP_2 and VP_3. **c** Charge stability diagram where an additional QD has been formed to the right of the DQD by raising the relevant tunnel barrier. The arrows indicate the position of the addition lines of the newly formed dot. **d** Differentiated demodulated charge sensor signal as a function of virtual plunger VP_4 and virtual barrier VB_4. The charge addition lines corresponding to the newly formed QD are clearly visible. No transitions of the pre-existing dots are observed, due to the use of virtual gates. **e** Visualization of the cross-capacitance matrix of the eight-dot array. The entries of each row show how the virtual plunger value (and hence the electrochemical potential) of a QD is influenced by other gate voltages. The rows for virtual barrier gates are omitted for simplicity. The plungers of both sensing dots are included in the matrix

only slightly affected, indicating the effectiveness of the virtual gate concept.

We complete the tuning of the newly formed dot to the single electron regime by measuring a charge stability diagram, here sweeping virtual plunger VP_4 versus virtual barrier VB_4. A set of diagonal lines indicates charge transitions of the newly formed QD (see Fig. 2d). We can identify the last charge transition in the bottom left of the figure. The cross-capacitance matrix is unchanged, $A_3 = A_2$.

Next, we update the cross-capacitance matrix (step 4). First, we fill the row corresponding to VP_4 in an otherwise unity matrix, which gives A_4'. The effect of all VP_j and VB_j on VP_4 is determined, as described for the first double dot, with the distinction that we now start from a set of virtual gates, expressed by matrix A_2. We then consolidate the virtual gates for dots 2–4 (and the first sensing dot) into the matrix $A_4 = A_4'A_3$.

Finally, in step 5, the matrix entries in A_4 are updated to account for reduced screening of the gate potentials when the two-dimensional electron gas at the location of QD_4 is depleted. To do so, we remeasure the cross-talk from all the virtual plunger and barrier gates to all the virtual plunger gates. This results in the matrix A_5', which represents a correction on A_4 and is constructed using the virtual gates expressed by A_4. Therefore, the updated cross-capacitance matrix A_5 is found by matrix multiplication, $A_5 = A_5'A_4$. Additional dots, including the second sensing dot, are formed by repeating steps 3 to 5.

Qubyte in the single electron regime

We apply the $n+1$ method to form a sextuple QD and octuple QD. We start with a DQD confined between the barrier gates B_1 and B_3 and initially extend the array to the right. The electrochemical potentials and thus the number of electrons residing on all QDs can be independently controlled. The results are verified by charge stability diagrams of neighboring pairs of virtual plunger gates, see Fig. 3b–f, where the sextuple dot has been initialized with one electron in each of the QDs. The gate voltages at the center of all of these plots are identical. All data sets have been acquired by fast voltage sweeps. Each plot can be interpreted as a charge stability diagram of a DQD, independent of the neighboring QDs. The virtual gates control the electrochemical potential of the DQD and the number of electrons can be determined easily from the measurements. This set of measurements contains the full information of the charge state of the sextuple QD and is much easier to interpret and work with than conventional charge stability diagrams, where multiple charge addition lines, as well as interdot transitions, are visible in a single plot. In fact, the data of Fig. 1b was taken for illustration purposes only, after forming the sextuple dot using measurements such as those in Fig. 3.

Following the same $n+1$ method, the sextuple QD is further extended to an octuple QD array by adding another QD on each side. Due to limitations of the experimental setup (see Methods section for details), the plunger gates P_1 and P_8 are not connected to high-frequency lines necessary to apply fast gate voltage sweeps. Therefore, any measurement using virtual gates involving these gates must rely on slow gate voltage sweeps. For this reason, we first formed a sextuple dot in the center and only then extended it to an octuple dot. Figure 3a, g show charge stability diagrams as a function of VP_1, VP_2 and VP_7, VP_8, respectively, completing the formation of the Qubyte register.

The cross-capacitance matrix for the octuple QD configuration of Fig. 3 is shown in Fig. 2e. It visualizes the effect of plunger and barrier gates on the electrochemical potential of all QDs. As discussed, each row has been normalized such that the diagonal elements are 1. In these units, the effect of the closest barrier gates on the electrochemical potential of a QD is typically between 0.9 and 1.1. This is in agreement with the device geometry (see Fig. 1a) where the barrier gates are 30 nm longer than the plunger gates, bringing them close to the expected QD position. The influence of a neighboring plunger gate on a dot potential is on the order of 0.4–0.5 and the one of the next-nearest neighbor 0.15–0.2, so the coupling diminishes with distance, as expected (Supplementary Fig. S2 plots the cross-capacitance versus distance). The cross-capacitance to the sensing dots is small

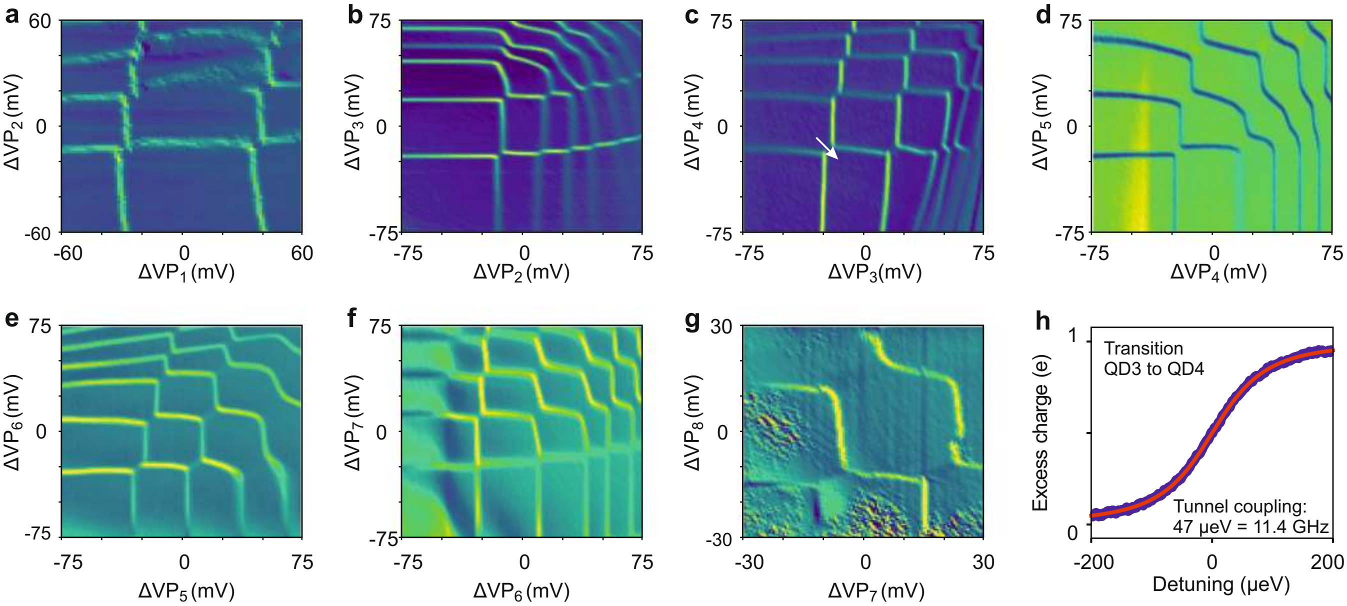

Fig. 3 Qubyte in the single electron regime. **a**–**g** Charge stability diagrams of pairs of neighboring QDs within the array. The differential demodulated voltage is plotted as a function of the virtual plunger gates. For panels **b**–**f**, the charge stability diagrams were measured with a sextuple QD defined between barrier gates B_1 and B_7. The measurements are centered around the single electron occupation. Panels **a**, **g** show charge stability diagrams of the two outermost DQDs of an octuple QD array. These panels took about 2 h each, compared to 10 s for the other panels, and may thus be more susceptible to background charge rearrangements. **h** Scan along the interdot detuning axis of QD_3 and QD_4 with one electron in those two dots (see arrow in **c**). The data has been fit according to the model described in refs [22,27]

(typically below 0.1), but nevertheless it is relevant to correct for, as the sensing dots are operated at a steep slope of a Coulomb peak to maximize the charge detection sensitivity.

By means of the virtual barrier gates VB_i, we can adjust the interdot tunnel couplings while cross-capacitance correction compensates the influence on the electrochemical potentials. To determine the interdot tunnel coupling, we measure the charge sensor response along the detuning axis across a single-electron transition. Figure 3h shows an example for the (1, 1, 0, 1, 1, 1)–(1, 0, 1, 1, 1, 1) transition, where the numbers in brackets indicate the number of charges on each of the six dots, from QD_2 to QD_7. The data is fit according to a simple model considering broadening of the transition due to tunnel coupling and thermal excitation,[22,27] using a measured effective electron temperature of $T_e = 90$ mK. The tunnel coupling for all pairs of neighboring dots has been tuned to a range of 5 to 15 GHz (see Supplementary Fig. S3).

To further verify the validity of the $n + 1$ method implemented via the use of virtual gates, we record the charge stability diagram of two neighboring dots, while all other dots are kept in Coulomb blockade. One by one we step the virtual plunger gates of the neighboring dots, which ideally should not affect the measured charge stability diagram. Figure 4 depicts such a test for QD_5 and QD_6. In panel (a) VP_4 has been increased compared to panel (b) and in panel (c) VP_7 has been increased. The charge stability diagram is not affected by small changes in neighboring electrochemical potentials, which implies that the virtual gates behave as expected and verifies that the charge stability diagram indeed shows addition lines of the expected dots. The 5 mV step size was chosen large enough such that the functioning (or not) of the virtual gates can be properly tested, while remaining well below half the addition energy. A step (positive or negative) of more than half the addition energy would change the electron occupation. The same measurements are repeated for all QDs; charge stability diagrams of neighboring QDs were measured while the electrochemical potential of all other QDs has been altered one by one. Data sets for all gate combinations are shown in Supplementary Fig. S4, showing similar results as presented in Fig. 4.

We note that it is not trivial that this method works flawlessly and care has to be taken to ensure the electron occupation of each dot is as intended. Specifically, it is important that the neighboring QDs remain sufficiently far from any charge transitions. This requires that the cross-capacitances are measured with a reasonable accuracy, and that the neighboring QDs be detuned from the Fermi level by more than the interdot capacitive coupling energy. To illustrate this point, a set of charge stability diagrams for QD_4 and QD_5 is shown in Fig. 5a–c, with increasing values for VP_6 per panel (The Supplementary video shows a similar series of charge stability diagrams in steps of 0.5 mV in VP_6.). Figure 5a shows a reference plot of a clean charge stability diagram. In Fig. 5b, the same gate voltages are scanned but VP_6 has been changed by 10 mV. Extra lines appear, which disappear again when increasing VP_6 further (Fig. 5c). The extra lines can be understood if we inspect the charge stability diagram for QD_5 and QD_6, which is depicted in Fig. 5d with arrows indicating the values of QD_6 used in panels (a–c). We see that arrow b, which corresponds to the case of Fig. 5b, passes through an interdot transition of QD_5 and QD_6, then intersects an addition line for QD_6 (since the virtual gates are not perfect, this addition line is slightly tilted) and finally cuts through another interdot transition of QD_5 and QD_6. These three crossings occur at the positions of the red circles in Fig. 5b. By comparison, arrows a and c do not pass through any charge transitions involving QD_6. This set of data makes clear how to avoid ambiguity in controlling and verifying the number of electrons on each dot.

We can observe the same effects in classical simulations of the charge stability diagrams. The simulation considers only three QDs and adopts the constant interaction model,[17] meaning the charging energies and capacitive interdot coupling energies are assumed to be constant. Imperfections of the cross-capacitance matrix are taken into account in the model. Other effects, e.g., tunnel coupling, non-linearities of the cross-talk and latching effects are neglected. Figure 5e shows a simulated charge stability diagram for QD_5 and QD_6, with the arrows a, b and c at similar locations as in the measurements of Fig. 5d. Figure 5f shows the simulated charge stability diagram for QD_4 and QD_5, for the case of arrow b. Similar to the data in Fig. 5b, we observe extra lines in the simulated charge stability diagram, as arrow b passes through interdot transitions and an addition line for QD_6. While details vary, in part because tunnel coupling is not included in the simulation, the simulation results are in good qualitative agreement with the experimental data.

DISCUSSION

We developed a powerful technique to tune an array of QDs one by one and load it in the few electron regime. We apply this method to tune up a linear array of eight quantum dots in GaAs from scratch.

All charge stability diagrams have been acquired by fast voltage sweeps. At low resolution and low averaging, sufficient for tuning purposes, the acquisition time per panel is on the order of a few 100 ms. High-quality data sets such as those shown in Fig. 3b–f take approximately 10 s per panel. Based on these time scales, creating a six-dot array following the $n + 1$ method, starting from measurement of the pinch-off characteristics of individual gates, currently takes one to two days for an experienced user and a well-behaved sample. This was confirmed on a second sample of

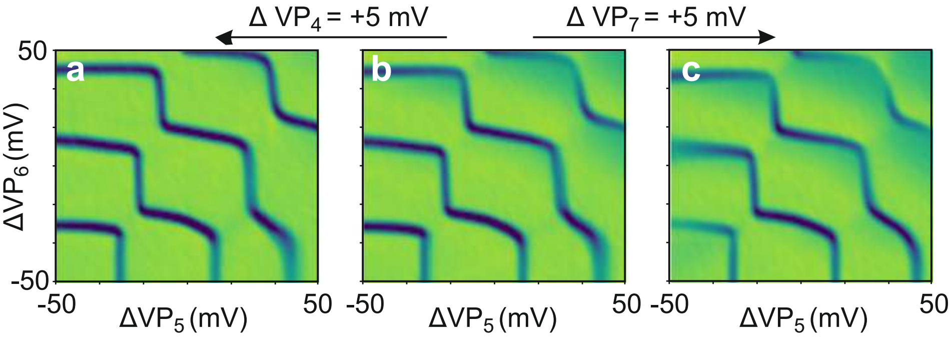

Fig. 4 Verifying independent control of the electrochemical potentials. Charge stability diagrams of QD_5 and QD_6 measured as function of the virtual plunger gates with all other QDs near the center of a charge stability region. Panel **b** is a reference measurement. Panel **a**, **c** are taken for identical gate voltages as **b** except that VP_4 (VP_7) is increased by 5 mV. We note that stepping VP_4 (VP_7) has almost no influence on the charge stability diagram of QD_5 and QD_6. This figure shows a subset of the data shown in Supplementary Fig. S4

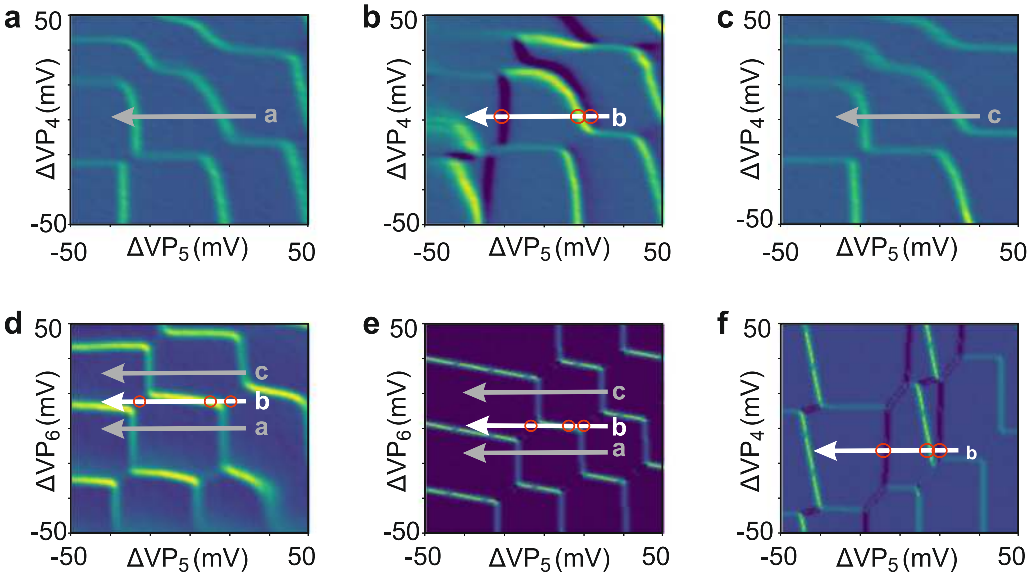

Fig. 5 Possible pitfalls when using virtual gates. **a**–**c** Charge stability diagrams of QD_5 and QD_4. The virtual plunger VP_6 is stepped by 10 mV from **a** to **b** and by another 15 mV from **b** to **c**. In **b**, additional lines appear, which arise both from interdot and dot-reservoir transitions, as explained in the text. **d** Charge stability diagram of QD_6 and QD_5. The arrows indicating cuts along the VP_5 axis for three different values of VP_6 correspond to the arrows in **a**–**c**. **e** Simulated double dot charge stability diagram computed for a triple quantum dot system. The simulation assumes the constant interaction model, taking into account the capacitive interdot coupling and using on purpose an imperfect cross-capacitance matrix. The simulation results exhibit similar features as the measurements in **d**. The three arrows are drawn at the corresponding locations as in **d** as well. **f** Simulated charge stability diagram computed for the same triple quantum dot as in **e**, but for the other DQD. Similar to the data in **b**, we observe several additional interdot and dot-reservoir charge transition lines

the same design. We did observe that not all lithographically similar devices are suitable to host eight QDs. During the initial DC characterization, in some devices not all QDs could be formed individually or some QDs seemed to be positioned under a gate instead of in the channel. We note that this failure mode can be identified at an early stage of measurements prior to running the $n+1$ method. On the other hand, the method can cope with limited uniformity in a device and a certain amount of disorder, as seen from the variation in the pinch-off voltages in Supplementary Table 1. Furthermore, the virtual gates technique facilitates tuning of the tunnel couplings, which we showed could be tuned to a relevant range for qubit operations in this device.

With regards to the scalability of this method, we make the following observations. First, the cross-capacitance quickly drops with distance between the gates and the dots. Therefore, only the entries near the diagonal of the cross-capacitance matrix are relevant and need to be determined. This implies a linear scaling of the number of cross-capacitance elements as a function of the number of dots. Second, as we relied on charge addition lines in charge stability diagrams of neighboring QDs to determine the number of electrons per dot, each of the QDs must be able to exchange electrons with at least one of the reservoirs. QDs not positioned at the end of the array need to exchange electrons via co-tunneling, mediated by a virtual occupation of the QDs in between.[17] The co-tunnel rate scales inversely proportional with the number of interdot tunnel barriers between a dot and the nearest reservoir, as well as with the detuning of the dots in between them.[28] As a result, we found that it was important to sufficiently open the existing interdot tunnel barriers before adding the last few dots, to avoid excessive latching effects. Once latching occurs, it becomes harder to reliably determine virtual gates and open the tunnel barriers. However, this is by no means a fundamental obstacle. When dots are formed one at a time, the newly formed dot is immediately adjacent to a reservoir and can thus be easily loaded. For dots in the interior, the $n+1$ method we introduced in principle takes care of maintaining their occupation through cross-talk compensation. If desired, verifying the dot occupation in the interior of a long array after it is formed can still be done, for instance by emptying the array (while not removing it), followed by sequential tunneling of electrons to the desired locations.[25] Finally, we believe that the $n+1$ method is not bound to a specific device geometry or material. In particular, it is directly applicable to linear arrays in silicon based QD devices[26] and can be extended to two-dimensional QD arrays. The $n+1$ method can become a standard method to conveniently tune QD arrays and should lend itself well to automation.[29,30]

The data also shows the limitations of the current approach. We correct for the cross-capacitance of plunger and barrier gates influencing electrochemical potentials but not for the influence on tunnel barriers. As a consequence, altering a virtual plunger gate will affect neighboring barriers, as can be seen in Fig. 3b. Increasing VP_2 and VP_3 increases the interdot tunnel coupling, which can be deduced from the broadening of the interdot transitions. In principle cross-capacitance effects on barriers can also be taken into account, as was demonstrated recently for a triple dot array.[22] However, this task is not trivial since the dependence of gate voltage to tunnel coupling is typically exponential and thus the linear approximation of the cross-capacitance matrix is only valid over a limited voltage range. As we have shown in this work, adjusting the interdot tunnel couplings individually is not a very difficult task, and this can be implemented using automated tuning algorithms as well.[31]

Altogether, the $n+1$ method shown here enables future experiments involving increasing numbers of electron spin qubits in semiconductor quantum dot arrays. It addresses an important bottleneck in scaling up quantum dot arrays and highlights the potential of this approach for large-scale quantum computation and simulation.

METHODS

The sample is fabricated from a silicon-doped GaAs/AlGaAs quantum well grown by molecular beam epitaxy. A two-dimensional electron gas is formed 90 nm below the surface. It shows a mobility of 1.6×10^6 cm^2/Vs at an electron density of $1.9 \times 10^{11}\,\mathrm{cm}^{-2}$. A single layer of metallic gates (Ti/Au), defined by electron-beam lithography, is biased with appropriate voltages to selectively deplete the 2DEG underneath. During cooldown the gates have been biased individually with positive voltages between +50 and +250 mV to reduce charge noise[18,19] and to improve the uniformity of the pinch-off characteristics of the gates. Details on bias cooling and pinch-off voltages are shown in Supplementary Table 1. On a second device where we successfully applied the $n+1$ method, we used a uniform bias cooldown voltage.

Plunger gates P_2 to P_8 of the array and the plunger gates of both sensing dots (X_1, X_2) are connected to bias-tees on the printed circuit board with a cut-off frequency of $f_C \approx 0.3$ Hz. This allows combining DC voltages and nanosecond gate voltage pulses on the same gate. Due to limitations of the experimental setup only eight gates (P_2 - P_7, X_1, X_2) could be connected to high-frequency lines. The bias-tee at P_8 limits the bandwidth to 0.3 Hz. Low-pass filtered DC lines are connected to P_1 ($f_C \approx 150$ kHz) and all barrier gates ($f_C \approx 5$ kHz).

Except for the initial characterization using DC transport, RF reflectometry is used, enabling fast, simultaneous read out of both charge sensors by frequency multiplexing.[32,33] As the capacitive coupling and thus the sensitivity decreases with distance from the sensor, we read out both sensors simultaneously to maximize the readout quality. The charge stability diagrams shown in Figs. 2–5 show the signal from the nearest charge detector. The sum of the derivative along both axis is plotted. In Fig. 1b, the signals from the two charge sensors are added. LC tank circuits based on home-built superconducting NbTiN inductors are connected to the ohmic contacts of the sensing dots (see labels RF in Fig. 1a). RF tones close to the resonance frequencies of the tank circuits, at 108.5 MHz and 171.9 MHz, are sent to the sample. The reflected signal is amplified at 4 K and at room temperature, I/Q demodulated to baseband, filtered with a 1 MHz low-pass filter, and recorded with a fast data acquisition card.

Data has been acquired and analyzed using the open source python packages QCoDeS available at https://qcodes.github.io/Qcodes and QTT (Quantum Technology Toolbox) available at https://github.com/QuTech-Delft/qtt.

DATA AVAILABILITY

Datasets and analysis scripts supporting the findings of this study are available at https://doi.org/10.5281/zenodo.2620418.[34]

ACKNOWLEDGEMENTS

We thank Floor van Riggelen and Luc Blom for software support and Raymond Schouten for electronics support. We thank all members of the QuTech spin qubit group for fruitful discussions. We acknowledge support by the Netherlands Organization of Scientific Research (NWO) Vici program, a supplement for Topconsortia for Knowledge and Innovation (TKI) of the Dutch Ministry of Economic Affairs, the Swiss National Science Foundation (SNF), and the QuantERA ERA-NET Cofund in Quantum Technologies implemented within the European Union's Horizon 2020 Programme, and a Japan Society for the Promotion of Science (JSPS) Postdoctoral Fellowship for Research Abroad. This research was sponsored by the Army Research Office (ARO) under grant numbers W911NF-17-1-0274 and W911NF-12-1-0607. The views and conclusions contained in this document are those of the authors and should not be interpreted as representing the official policies, either expressed or implied, of the ARO or the US Government. The US Government is authorized to reproduce and distribute reprints for government purposes notwithstanding any copyright notation herein.

AUTHOR CONTRIBUTIONS

C.V. and A.M.J.Z. performed the experiment, following preliminary experiments by T. H and T.F., and analyzed the data. C.V., A.M.J.Z., P.T.E., C.J.v.D. and L.M.K.V. discussed the data. U.M. and J.P.D designed and fabricated the samples. C.R. and W.W. grew the heterostructure. C.V., A.M.J.Z. and L.M.K.V. wrote the manuscript with input from all authors. L.M.K.V. initiated and supervised the project. C.V. and A.M.J.Z. contributed equally to this work.

ADDITIONAL INFORMATION

Supplementary information accompanies the paper on the *npj Quantum Information* website (https://doi.org/10.1038/s41534-019-0146-y).

Competing interests: The authors declare no competing interests.

Publisher's note: Springer Nature remains neutral with regard to jurisdictional claims in published maps and institutional affiliations.

REFERENCES

1. Loss, D. & DiVincenzo, D. P. Quantum computation with quantum dots. *Phys. Rev. A* **57**, 120–126 (1998).
2. Hanson, R., Kouwenhoven, L. P., Petta, J. R., Tarucha, S. & Vandersypen, L. M. K. Spins in few-electron quantum dots. *Rev. Mod. Phys.* **79**, 1217–1265 (2007).
3. Vandersypen, L. M. K. et al. Interfacing spin qubits in quantum dots and donors - hot, dense and coherent. *npj Quantum Inf.* **3**, 34 (2017).
4. Yoneda, J. et al. A quantum-dot spin qubit with coherence limited by charge noise and fidelity higher than 99.9%. *Nat. Nanotech.* **13**, 102–106 (2018).
5. Nowack, K. C. et al. Single-shot correlations and two-qubit gate of solid-state spins. *Science* **333**, 1269–1272 (2011).
6. Shulman, M. D. et al. Demonstration of entanglement of electrostatically coupled singlet-triplet qubits. *Science* **336**, 202–205 (2012).
7. Veldhorst, M. et al. A two-qubit logic gate in silicon. *Nature* **526**, 410–414 (2015).
8. Zajac, D. M. et al. Resonantly driven CNOT gate for electron spins. *Science* **359**, 439–442 (2018).
9. Huang, W. et al. Fidelity benchmarks for two-qubit gates in silicon. *Preprint at: arXiv:1805.05027* (2018).
10. Xue, X. et al. Benchmarking gate fidelities in a Si/SiGe two-qubit device. *Preprint at: arXiv:1811.04002* (2018).
11. Watson, T. F. et al. A programmable two-qubit quantum processor in silicon. *Nature* **555**, 633–637 (2018).
12. Thalineau, R. et al. A few-electron quadruple quantum dot in a closed loop. *Appl. Phys. Lett.* **101**, 103102 (2012).
13. Takakura, T. et al. Single to quadruple quantum dots with tunable tunnel couplings. *Appl. Phys. Lett.* **104**, 113109 (2014).
14. Fujita, T., Baart, T. A., Reichl, C., Wegscheider, W. & Vandersypen, L. M. K. Coherent shuttle of electron-spin states. *npj Quantum Inf.* **3**, 22 (2017).
15. Mukhopadhyay, U., Dehollain, J. P., Reichl, C., Wegscheider, W. & Vandersypen, L. M. K. A 2 × 2 quantum dot array with controllable inter-dot tunnel couplings. *Appl. Phys. Lett.* **112**, 183505 (2018).
16. Mortemousque, P. A. et al. Coherent control of individual electron spins in a two dimensional array of quantum dots. Preprint at: *arXiv:1808.06180* (2018).
17. van der Wiel, W. G. et al. Electron transport through double quantum dots. *Rev. Mod. Phys.* **75**, 1–22 (2002).
18. Pioro-Ladrière, M. et al. Origin of switching noise in GaAs/Al$_x$Ga$_{1-x}$As lateral gated devices. *Phys. Rev. B* **72**, 115331 (2005).
19. Buizert, C. et al. Insitu reduction of charge noise in GaAs/Al$_x$Ga$_{1-x}$As schottky-gated devices. *Phys. Rev. Lett.* **101**, 226603 (2008).
20. Yang, C. H. et al. Charge state hysteresis in semiconductor quantum dots. *Appl. Phys. Lett.* **105**, 183505 (2014).
21. Ito, T. et al. Detection and control of charge states in a quintuple quantum dot. *Sci. Rep.* **6**, 39113 (2016).
22. Hensgens, T. et al. Quantum simulation of a fermi-hubbard model using a semiconductor quantum dot array. *Nature* **548**, 70–73 (2017).
23. Medford, J. et al. Quantum-dot-based resonant exchange qubit. *Phys. Rev. Lett.* **111**, 050501 (2013).
24. Malinowski, F. K. et al. Fast spin exchange between two distant quantum dots. *Nat. Commun.* **10**, 1196 (2019).
25. Baart, T. A. et al. Single-spin CCD. *Nat. Nanotech.* **11**, 330–334 (2016).
26. Mills, A. R. et al. Shuttling a single charge across a one-dimensional array of silicon quantum dots. *Nat. Commun.* **10**, 1063 (2019).
27. DiCarlo, L. et al. Differential charge sensing and charge delocalization in a tunable double quantum dot. *Phys. Rev. Lett.* **92**, 226801 (2004).
28. Braakman, F. R., Barthelemy, P., Reichl, C., Wegscheider, W. & Vandersypen, L. M. K. Long-distance coherent coupling in a quantum dot array. *Nat. Nanotech.* **8**, 432–437 (2013).
29. Baart, T., Eendebak, P. T., Reichl, C., Wegscheider, W. & Vandersypen, L. M. K. Computer-automated tuning of semiconductor double quantum dots into the single-electron regime. *Appl. Phys. Lett.* **108**, 213104 (2016).
30. Botzem, T. et al. Tuning methods for semiconductor spin qubits. *Phys. Rev. Appl.* **10**, 054026 (2018).
31. Van Diepen, C. J. et al. Automated tuning of inter-dot tunnel coupling in double quantum dots. *Appl. Phys. Lett.* **113**, 033101 (2018).
32. Barthel, C. et al. Fast sensing of double-dot charge arrangement and spin state with a radio-frequency sensor quantum dot. *Phys. Rev. B* **81**, 161308 (2010).
33. Hornibrook, J. M. et al. Frequency multiplexing for readout of spin qubits. *Appl. Phys. Lett.* **104**, 103108 (2014).
34. Volk, C. et al. Loading a quantum-dot based "Qubyte" register. Datasets and scripts. *Zenodo*. https://doi.org/10.5281/zenodo.2620418 (2019).

Open Access This article is licensed under a Creative Commons Attribution 4.0 International License, which permits use, sharing, adaptation, distribution and reproduction in any medium or format, as long as you give appropriate credit to the original author(s) and the source, provide a link to the Creative Commons license, and indicate if changes were made. The images or other third party material in this article are included in the article's Creative Commons license, unless indicated otherwise in a credit line to the material. If material is not included in the article's Creative Commons license and your intended use is not permitted by statutory regulation or exceeds the permitted use, you will need to obtain permission directly from the copyright holder. To view a copy of this license, visit http://creativecommons.org/licenses/by/4.0/.

© The Author(s) 2019